JJMIE

Volume 4, Number 5, November 2010
ISSN 1995-6665
Pages 553 - 566

Jordan Journal of Mechanical and Industrial Engineering

Numerical Modelling of a Turbocharger Splitter-Vaned Centrifugal Impeller at off-Design Conditions, Part I: Impeller Flow Field

A. Fatsis [a,*], A. Panoutsopoulou[b], N. Vlachakis [b]

[a] Technological University of Chalkis, Department of Mechanical Engineering, 34400 Psachna Evoias, Greece.

[b]Hellenic National Defence Systems S.A., 1, Ilioupoleos Avenue, 17236, Greece

Abstract

The 3D unsteady flow field in a centrifugal impeller with splitter vanes, due to a downstream static pressure distortion imposed by the volute collector at off-design operations, is analysed by means of numerical modelling. Two cases are examined: one analysing the impeller flow field at higher than nominal mass flows and one at lower than nominal mass flows. The hub streamsurface, where the channel length is longer reacts with smoother changes with respect to the shroud. For both cases, it is demonstrated that the exit static pressure non-uniformity propagates upstream and creates unsteady flow in the channels between the impeller full blades and splitter vanes resulting in changes in incidence, velocity components and relative flow angles. In the higher mass flow case the unsteady phenomena are more pronounced.

Keywords: Unsteady Flow, Centrifugal Impeller, Splitter Blades, Static Pressure Distortion.

Nomenclature

c	Speed of sound
f	Frequency
t	Time
L	Length of blade channel
M	Mach number
N_{bl}	Number of blades
P	Static pressure
S_r	Strouhal number
V	Absolute velocity
Δt	Time step
Ω	Reduced frequency
α	Absolute flow angle
β	Relative flow angle
ρ	Density
ω	Non-dimensional rotational impeller speed

Superscripts

bl	Blade
spl	Splitter

Subscripts

ps	Blade or splitter pressure side
r	Radial
rel	Relative
ss	Blade or splitter suction side
z	Axial
θ	Circumferential
0	Total conditions
1	Impeller inlet
2	Impeller trailing edge

* Corresponding author. afatsis@tee.gr.

1. Introduction

Centrifugal compressor impellers often employ the use of splitter vanes in order to achieve the high pressure ratio for which they are designed, avoiding thus the chocking of the flow in the vicinity of the leading edge of the blades where the free surface for the flow between two consecutive blades is minimum, [1]. It is proven experimentally that when a centrifugal compressor impeller is followed by a non-axisymmetric volute operating at off-design conditions, the circumferential distribution at the diffuser outlet and at the diffuser inlet is not uniform, [2]. It was also found that the circumferentially non-uniform profile of the static pressure follows a rather saw-tooth distribution, with its peak value (in the case of higher mass flows) or its lowest value (in the case of lower mass flows) corresponding to the volute tongue position, [2].

The propagation of the outlet static pressure distortion towards the impeller inlet was confirmed in [3]. Sudden changes in the flow field observed at the volute tongue, result from two counter-rotating vortices (because the total vorticity has not yet changed) at the impeller inlet. At mass flows lower than the optimum one, one of the vortices creates counter-rotating flow resulting in an increased incidence. The other vortex causes a decrease in incidence. A similar phenomenon occurs at higher than the optimum mass flows.

A simple 1D model was presented to predict the impeller response due to the circumferential static pressure variation caused by the volute, [4]. The model is applicable only for incompressible flows and assumes a circumferentially constant relative outlet flow angle. This is in contrast to experimental observations in which circumferential variations in the relative outlet flow angle were reported [5].

Better predictions were obtained by 2*D* unsteady models, solving the 2*D* unsteady potential flow equations by means of singularity or finite element method, [6]. Incompressible flow calculations solving the 2*D* Navier-Stokes flow using the k-ε model for turbulence were also done, [7]. Quasi-3*D* unsteady models predict the unsteady flow variations in the blade to blade surface at the shroud [2]. All these models, however, fail to provide information about the 3 *D* effects in the impeller.

A 3D numerical model based on the Euler equations was developed in order to study the unsteady flow field inside the impeller due to a circumferential variation of the static pressure at the impeller outlet, for the case of full-bladed impellers, [8]. The modelling of unsteady flows using the Euler equations assumes that the main unsteady flow characteristics are dominated by the propagation of pressure waves across the flow field.

In the present study, the extension of the method is presented for the case of 3D centrifugal impellers with splitter vanes operating at circumferentially non-uniform static pressure. Computations are performed for centrifugal impeller with backward leaned blades for lower and higher mass flows. Results obtained show that the present model is able to handle the unsteady flow field inside the impeller full and splitter blades. The outlet static pressure non-uniformity propagates upstream and causes unsteady flow in the impeller and creates incidences variations upstream the impeller blades.

1.1. Numerical Method

The numerical model used to analyse the unsteady impeller flow field consists of the 3D Euler equations. These equations can accurately capture flows where viscous phenomena are limited in certain regions of the flow, and this makes them an attractive tool for the computation of the dynamic behaviour of the unsteady flow inside the impeller. Adopting the Euler equations means that the viscous terms from the full Navier-Stokes equations are neglected, and the transport of momentum and energy in the fluid is done only by means of convective fluxes. Since viscous forces are neglected, this implies that the considered model is not valid at relatively low rotational speed. Using the Euler equations compressible rotational flow, steady or unsteady flow fields can be calculated. Flow unsteadiness due to circumferential inlet and outlet pressure distortions is governed mainly by wave propagation and to a lesser extent by viscous phenomena. This justifies the use of an unsteady 3 *D* Euler solver instead of a full 3 *D* Navier-Stokes solver. This simplification results in an affordable computer time and gives useful information on the dynamics of the flow in the case where the impeller is not heavily loaded and flow separation is limited. The model was validated for the case of full-bladed centrifugal impeller, showing fairly good agreement against available experimental results in the literature and predicting the unsteady flow features that are in agreement with experimental investigations, [8].

The 3D Euler equations in non-dimensional form are written in conservative form in cylindrical coordinates, *(r,θ,z)* as follows:

$$\frac{\partial \vec{u}}{\partial t}+\frac{1}{r}\cdot\frac{\partial\left(r\,f(\vec{u})\right)}{\partial r}+\frac{1}{r}\cdot\frac{\partial\, g(\vec{u})}{\partial\theta}+\frac{\partial\, h(\vec{u})}{\partial z}+\vec{b}(u)=0 \tag{1}$$

where $\vec{u}$ is the vector of conservative variables, $f(\vec{u}), g(\vec{u}), h(\vec{u})$ are the vectors of convective fluxes and $b(\vec{u})$ is the source term, defined in detail in [8].

The space discretization of the equations is done by means of the finite volume technique. More specifically the bitrapezoidal cell, Figure 1, was used, offering second order spatial accuracy in smooth grids, [9].

The partial differential equations are written in a semi-discrete form as follows:

$$\frac{d}{d\,t}\left(\vec{u}\right)+\vec{R}=0 \tag{2}$$

where R are the residuals of the equations. Since the purpose of this study is the calculation of unsteady flows, the choice of the time integration scheme has a significant role on the accuracy of the results.The Runge-Kutta four steps scheme, providing second order accuracy for non-linear partial differential equations and extensive stability limits up to a CFL number of $2\cdot\sqrt{2}$, was used for this purpose.

$$\begin{aligned}
\vec{u}^{(0)} &= \vec{u}^{n}\\
\vec{u}^{(1)} &= \vec{u}^{(0)}-\frac{\Delta t}{2}\cdot\vec{R}^{(0)}\\
\vec{u}^{(2)} &= \vec{u}^{(0)}-\frac{\Delta t}{2}\cdot\vec{R}^{(1)}\\
\vec{u}^{(3)} &= \vec{u}^{(0)}-\Delta t\cdot\vec{R}^{(2)}\\
\vec{u}^{(4)} &= \vec{u}^{(0)}-\frac{\Delta t}{6}\cdot\left(\vec{R}^{(0)}+2\cdot\vec{R}^{(1)}+2\cdot\vec{R}^{(2)}+\vec{R}^{(3)}\right)\\
\vec{u}^{n+1} &= \vec{u}^{(4)}
\end{aligned} \tag{3}$$

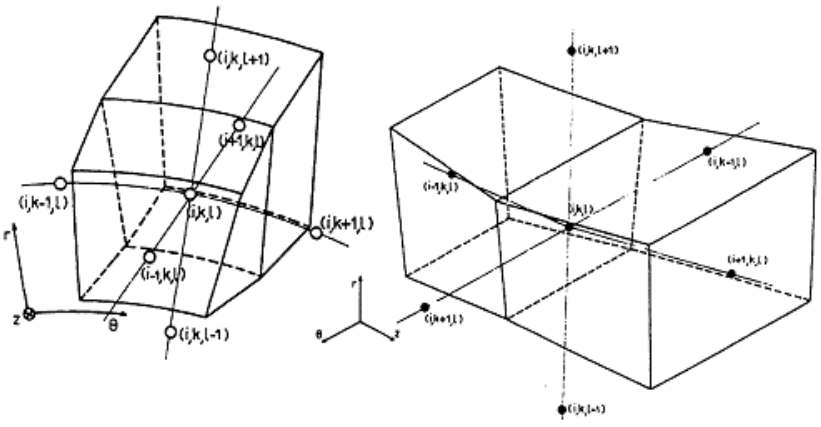

Figure 1: The bitrapezoidal volume used for the space discretisation

Extensive testing of the method in special test cases for which analytical solutions exist, has demonstrated the accuracy of this scheme for unsteady flow predictions, [2].

Impermeable wall boundary conditions are imposed on the solid walls (i.e. on the blade and splitter suction and pressure side and on the hub and shroud walls) by considering only the static pressure when computing the convective fluxes. The evaluation of the artificial dissipation on the solid walls is done by means of higher order extrapolation polynomials in order to minimize the dissipative fluxes, [8]. At the inflow and outflow boundaries, non-reflecting boundary conditions based on the Fourier decomposition, were used, [8]. Non-reflecting boundary conditions suggest infinitely long pipes upstream and downstream of the impeller and it is shown in [8] that the solution is not affected by the upstream location of the inflow boundary.

The physical boundary conditions specified upstream assuming subsonic inflow, are: Total pressure, total temperature and two flow angles (4 physical boundary conditions). The fifth boundary condition is a numerical one coming from the interior point of the computational domain.

The physical boundary condition specified downstream assuming subsonic outflow, is taken to be the static pressure (1 physical boundary condition required). The rest four boundary conditions are numerical ones coming from the interior point of the computational domain.

Since the outflow static pressure is not uniform along the circumference, this means that as the impeller rotates, a virtual point attached at the trailing edge experiences different values of the static pressure through out a full rotation, which consists the period of the phenomenon. Phase-lagged periodicity conditions were used to simulate this non-uniformity and to compute the fluxes through the upstream and downstream streamlines.

An H-grid was used for the calculations. A projection of this grid in the meridional plane (r-z) and in the blade-to-blade plane (θ-z), as well as a three-dimensional view of some of the impeller blades is given in Figure 2.

The unsteadiness of the incompressible flow in a channel of length L is normally characterized by the reduced frequency,

$$\Omega = \frac{f \cdot L}{V} \tag{4}$$

where V is the speed by which a particle is transported through the channel. In Turbo-

machinery applications, L is normally defined as the length of a blade passage, whereas f is the number of rotations per second times the number of perturbation waves around the circumference.

The acoustic Strouhal number is more appropriate to characterize compressible flows. It is defined as the product of the reduced frequency and the Mach number:

$$S_r = \Omega \cdot M = \frac{f \cdot L}{c} \tag{5}$$

It relates the time needed by a pressure wave to travel a distance L, at the speed of sound c to the period of the pressure perturbation 1/f. Unsteady effects are small for Sr < 0.1 and the flow can be evaluated by means of steady calculations. For Sr > 0.1 accurate results can be obtained only by means of unsteady flow calculations.

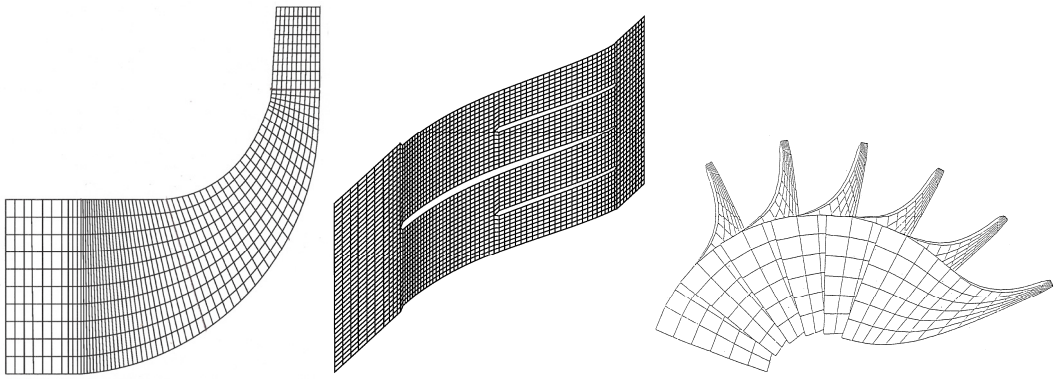

Figure 2: (a)Meridional *(r-z), (b)*Blade-to-blade *(θ-z)* view of the H-grid used for the calculations, (c)Three-dimensional view of some of the impeller blades

2. Impeller flow analysis

2.1. Mach number distributions at lower than optimum mass flows

The centrifugal impeller analysed has 10 full backward leaned blades and 10 splitter vanes. The circumferential static pressure distribution specified at the downstream boundary, shown in Figure 3, is typical for lower (Figure 3a) and higher (Figure 3b) than nominal flow rates.

A blade-to-blade projection of the numerical domain used at shroud streamsurface, is shown in Figure 4. Dashed lines define the lower channel between the blade suction side and the splitter vane pressure side. Continuous lines define the upper channel between the splitter vane suction side and the full blade pressure side.

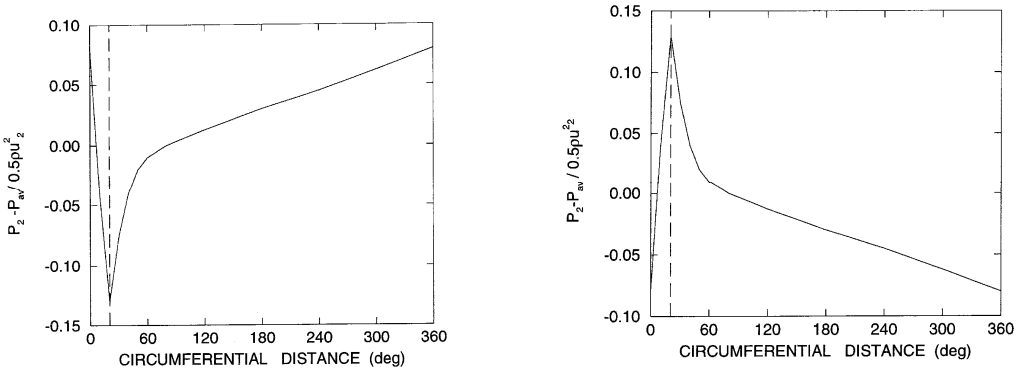

(a) (b)

Figure 3: Circumferential outlet static pressure distribution at (a) lower than optimum mass flows and (b) at higher mass flows (- - - tongue position)

Phase-lagged periodicity conditions are used to update the upstream and downstream stagnation pseudo-streamlines AB, CD and EF, GH, respectively. The points along the pseudo-streamlines upstream and downstream of the splitter vanes (namely KL, MN in Figure 4) are treated as interior points of the numerical domain and simple continuity of the fluxes is imposed.

The acoustic Strouhal number based on the length of the full blade, as defined by equation (5), is $S_r^{bl} = 0.22$, while the acoustic Strouhal number based on the length of the splitter vane is $S_r^{spl} = 0.146$.

Unsteady flow calculations begin having as initial guess the steady state converged solution at $t = t_0$. Convergence to a periodic state is reached when the calculated flow field repeats itself after every rotation of the impeller (which corresponds to several hundred computations). The distribution of the relative blade Mach number at shroud, mean and hub for the full blades and the splitter vanes is plotted on Figures 5–7 for different angular positions, θ, around the circumference. The dashed lines indicate the Mach number on the surfaces indicated with dashed lines on Figure 4 (lower channel). The continuous lines show the Mach numbers in what is called the upper channel.

The low back pressure at θ = 45° results in a local increase of mass flow, propagating upstream as an expansion wave. At θ = 90° it has reached the leading edge of the splitter where it results in a small incidence, shown by the small differences between the suction and pressure side Mach number at leading edge. It reaches the full blade leading edge at θ = 135°, where the smallest difference between the suction and pressure side Mach number is observed.

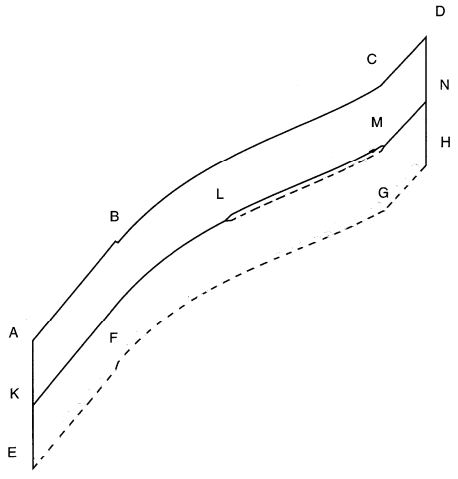

Figure 4: Blade-to-blade projection of the computational domain used for the splitter-vaned impeller computations

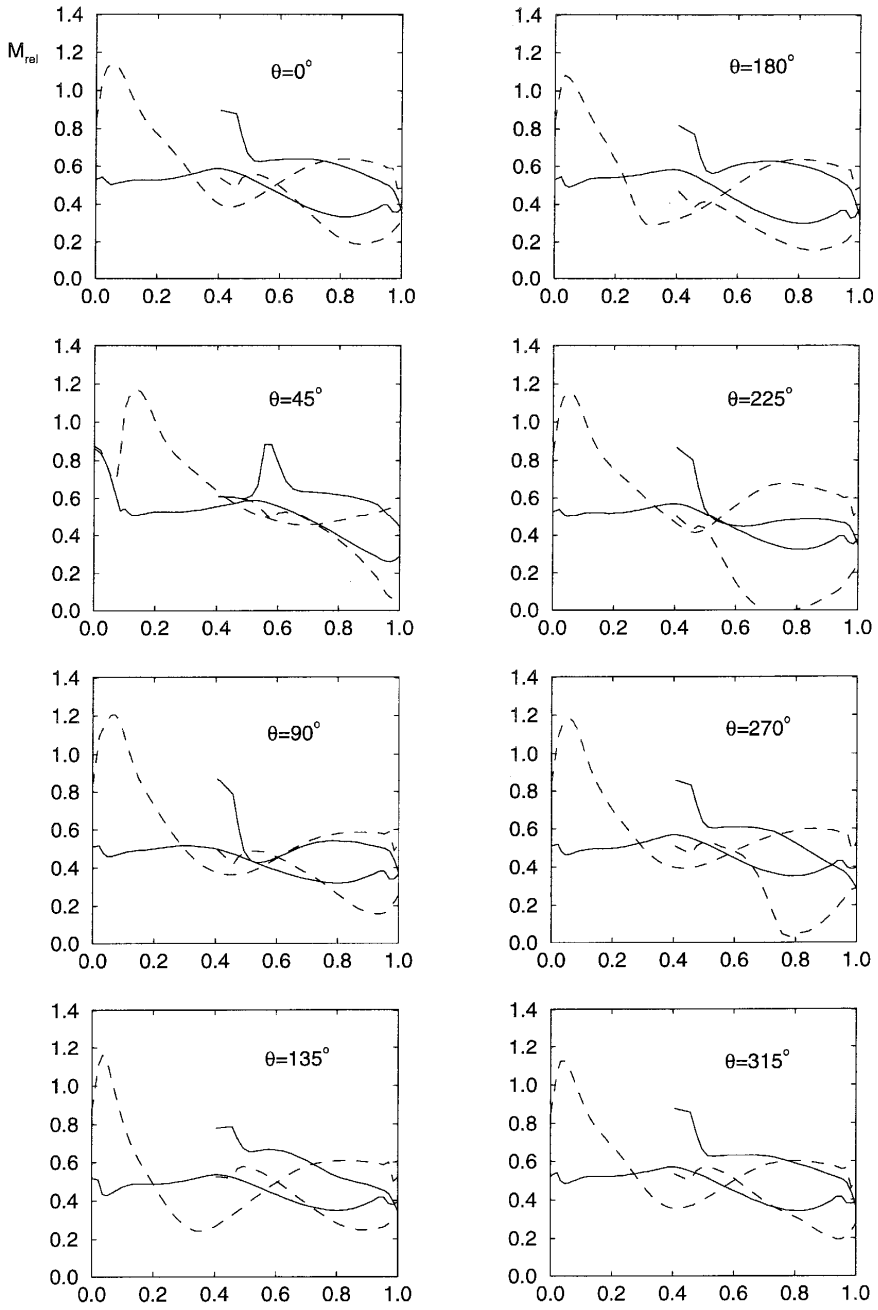

Figure 5: Blade relative Mach number versus the blade length at shroud streamsurface for the lower mass flow case during one rotation. Dashed lines illustrate the distribution in the lower channel of figure 4 and continuous lines the distribution in the upper channel of figure 4.

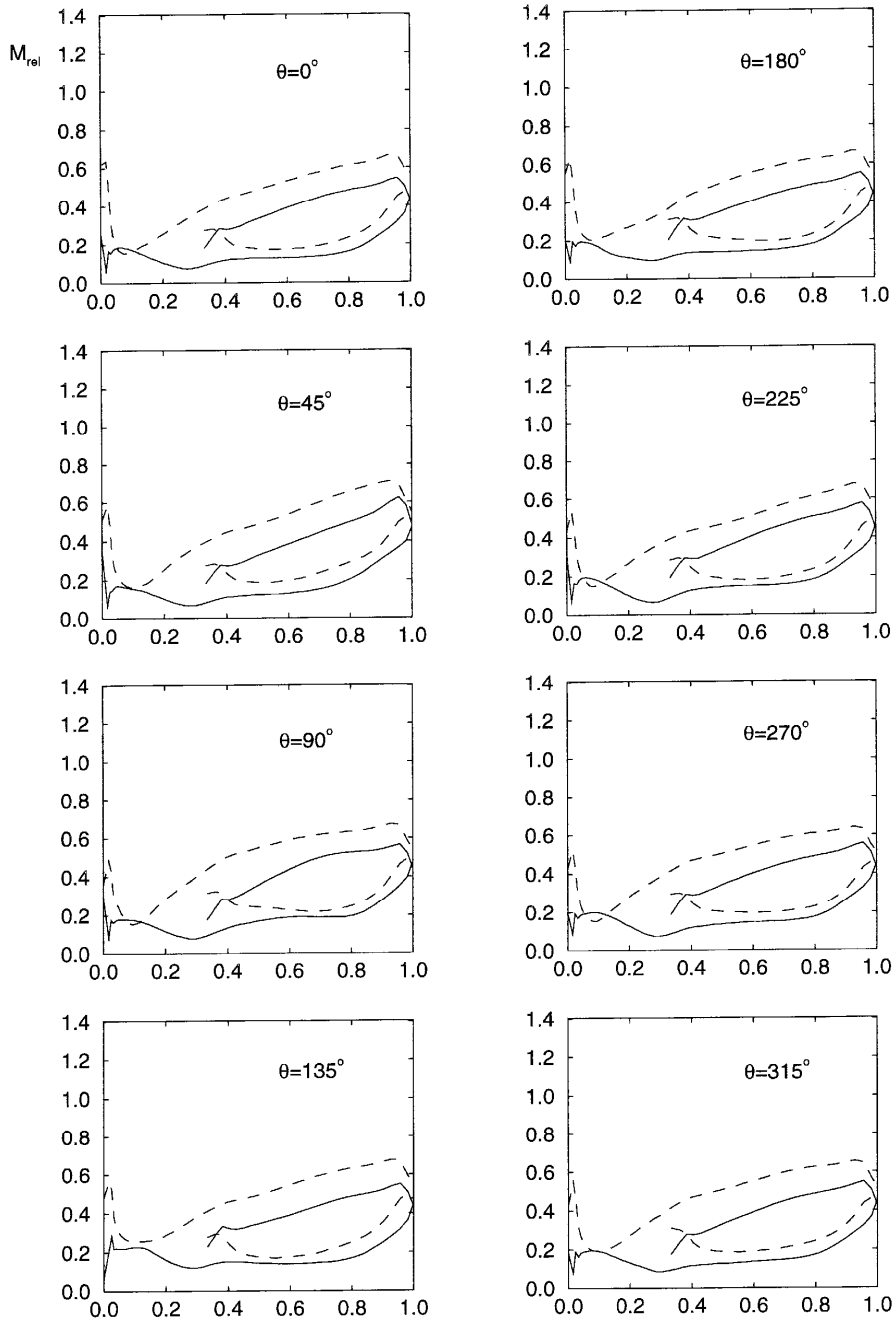

Figure 6: Blade relative Mach number versus the blade length at mean streamsurface for the lower mass flow case during one rotation. Dashed lines illustrate the distribution in the lower channel of figure 4, and continuous lines the distribution in the upper channel of figure 4.

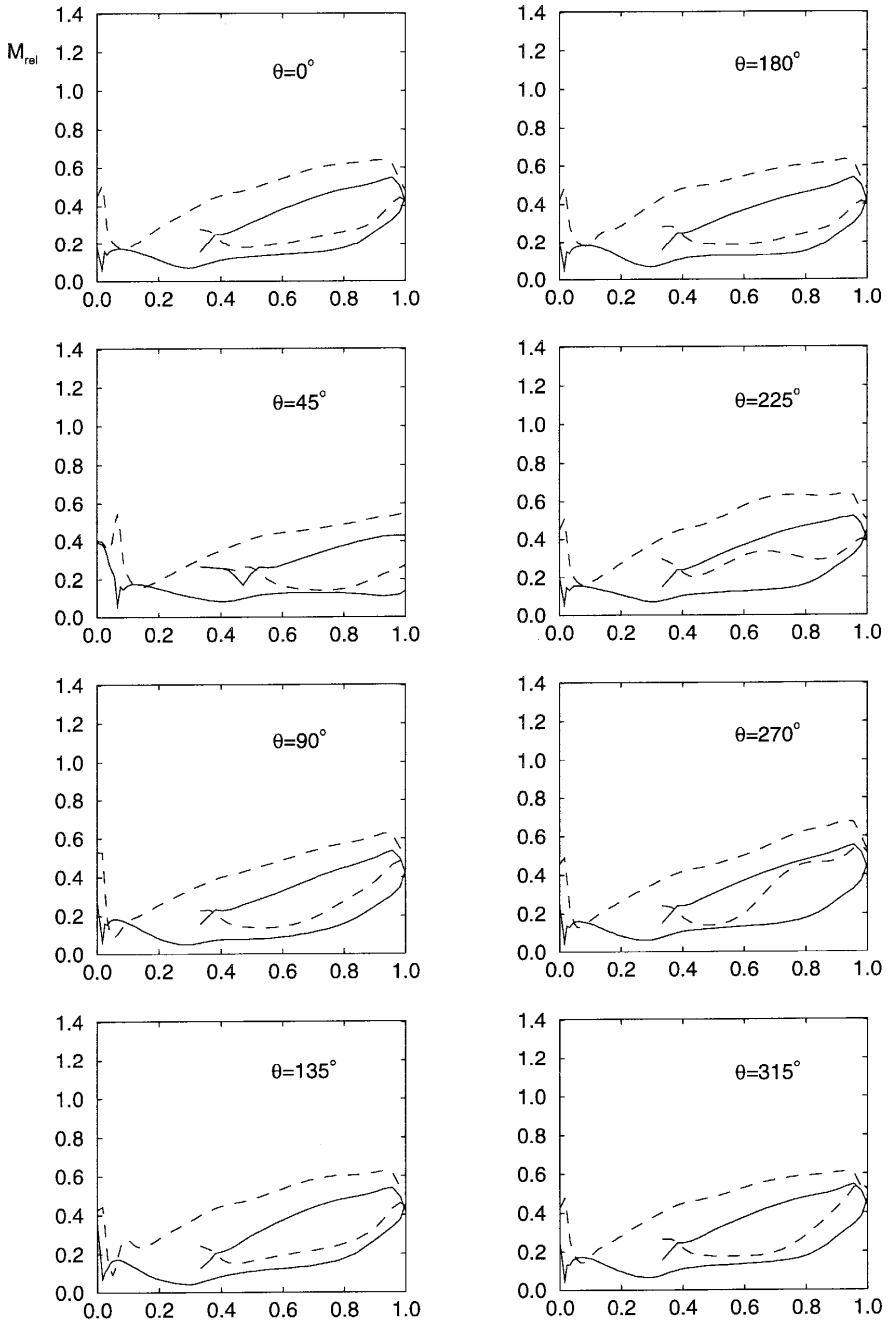

Figure 7: Blade relative Mach number versus the blade length at hub streamsurface for the lower mass flow case during one rotation. Dashed lines illustrate the distribution in the lower channel of figure 4, and continuous lines the distribution in the upper channel of figure 4.

In the mean time a pressure wave resulting from the sudden pressure increase between $\theta = 30^o$ and $\theta = 90^o$ has started to move upstream. It reaches the leading edge of the splitter at $\theta = 135^o$, where it creates a high splitter vane suction side Mach number because of the high incidence. The same pressure wave reaches the full blade leading edge at $\theta = 180^o$ and 225^o where the suction side Mach number has its maximum.

From the value of the acoustic Strouhal number, one can conclude that it takes half a rotation for a wave to move from trailing edge to leading edge and back, so that a pressure wave travels twice forth and back during one rotation (the second time at lower amplitude because of damping). This is confirmed by the similarity between the

left and the right column of Figure 5 indicating that the relative Mach number distribution is almost repeating itself every 180^o. Variations in blade loading in transonic regime due to static pressure distortion were also calculated in [12]. In that article it was also concluded that the unsteadiness influences the impeller flow field and creates acoustic wave structures inside the impeller.

The variations of Mach number are much smaller on the mean streamsurface (Figure 6). The changes in blade loading are mainly due to variations of the suction side Mach number distribution. The pressure side distribution shows almost no variations. A twice per rotation variation of the incidence can be concluded from the variation of the full blade suction side Mach number near to leading edge. Observations from the results of [12] confirm that the mean streamsurface reacts less that the shroud streamsurface.

The relative Mach number distribution at hub is shown in Figure 7. In this figure a given blade passage between two consecutive full blades is captured as it rotates around the circumference. The circumferential angle, θ, of the passage varies from 0 to 360 degrees. Eight different circumferential positions were selected, having a peripheral increment of 45 degrees each. From that figure one can see that the Mach number at blade suction side at shroud is slightly higher than one, indicating a transonic area standing at the suction side area. After a peak in the suction side Mach number due to incidence, a nearly constant loading of the full and splitter vanes is observed. Since the suction side Mach number remains supersonic for all values of the circumferential angle, θ, the downstream static pressure distortion cannot propagate upstream at the shroud radius. This means that the upstream-propagating pressure waves are reflected at the transonic area and they return downstream affecting the loading of the splitter vanes. One observes a periodic variation of the Mach number at the suction side leading edge and at 30% of the blade length. The lower blade channel has a higher Mach number.

2.2. Inlet and outlet flow distortion at lower than optimum mass flow

In Figure 8 one can see the mass averaged variation of the relative flow angle, β_2, the absolute flow angle α_2, and the non-dimensional radial and absolute tangential flow velocity components, V_{R2} and $V_{\theta 2}$ downstream the trailing edge, at R/R2 = 1.10. The circumferential distance of 20o corresponds to the volute tongue position where the static pressure reaches a minimum value on the outlet boundary (Figure 3a). The minimum value of $\beta_2, \alpha_2, V_{R2}$ and $V_{\theta 2}$ is not at 20o, but approximately at 40o because some time is needed by the pressure waves to travel from the outlet of the computational domain to the trailing edge position. For circumferential distances larger than 100o where the rate of increase of static pressure is small, no significant variations in β_2 are observed, except a second small minimum at 230o. This minimum can be seen well on the α_2 distribution (Figure 8b). The distributions of V_{R2} and $V_{\theta 2}$ follow the trend of the previous two distributions. However $V_{\theta 2}$ shows a sharp increase and decrease whereas V_{R2} shows only a sudden decrease.

Superposed on the variation with length $\Delta\theta = 180o$, one also observes a small variation with a length $\Delta\theta = 90o$, resulting from the reflection of the waves at the splitter vane leading edge.

Stars indicate the outlet flow conditions obtained from steady flow calculations, in which the local static pressure is imposed at the outlet. They show a monotonic increase or decrease with the outlet static pressure, but completely fail to capture the large local variations of the flow parameters.

The circumferential variation of the flow variables at the leading edge (Figure 9) also shows a 180o period. As it was observed in experiments [13], the static pressure variation propagates upstream and influences the whole impeller flow. Variations of the absolute flow angle α_1 and the absolute tangential and radial velocity components $V_{\theta 1}$ and V_{Z1} show variations, which can be related to each other. The β_1 variation is completely different. Changes in the sign of α_1 and $V_{\theta 1}$, indicate the presence of two counter rotating vortices upstream of the leading edge, as was observed in [3]. The β_1 variation is a result of it. The upstream vortices have to be counter rotating because no net vorticity has been created yet, upstream of the leading edge. Numerical simulations using a Navier-Stokes commercial code for the case of impeller-volute interaction [14] reported discrepancies between experimental and numerical data due to the jet and wake structure between the impeller blades and due to the difficulty to have a turbulence model to treat the flow separation at the blade suction side.

2.3. Inlet and outlet flow distortion at higher than optimum mass flow

The circumferential outlet static pressure distortion for higher than nominal mass flow is shown in Figure 10. It was concluded in [15] that both in case of lower and of higher mass flows, the circumferential static pressure distortion causes unsteady impeller flow field. The relative blade Mach number distribution at hub, mean and shroud

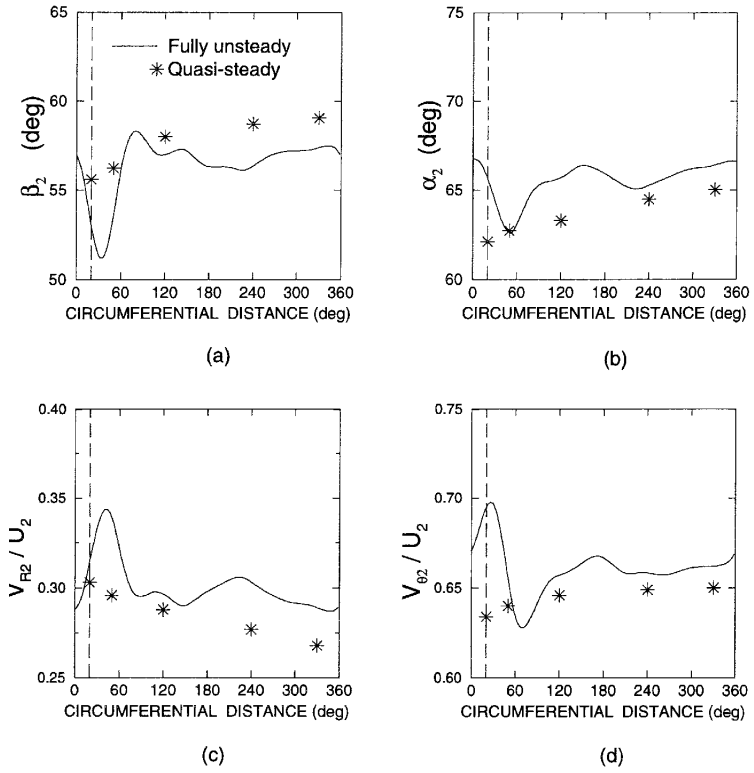

Figure 8: Circumferential variation of mass averaged $\beta_2, \alpha_2, V_{R2}, V_{\theta 2}$ at R/R_2=1.10, S_r=0.22, for the lower mass flow case (- - - tongue position)

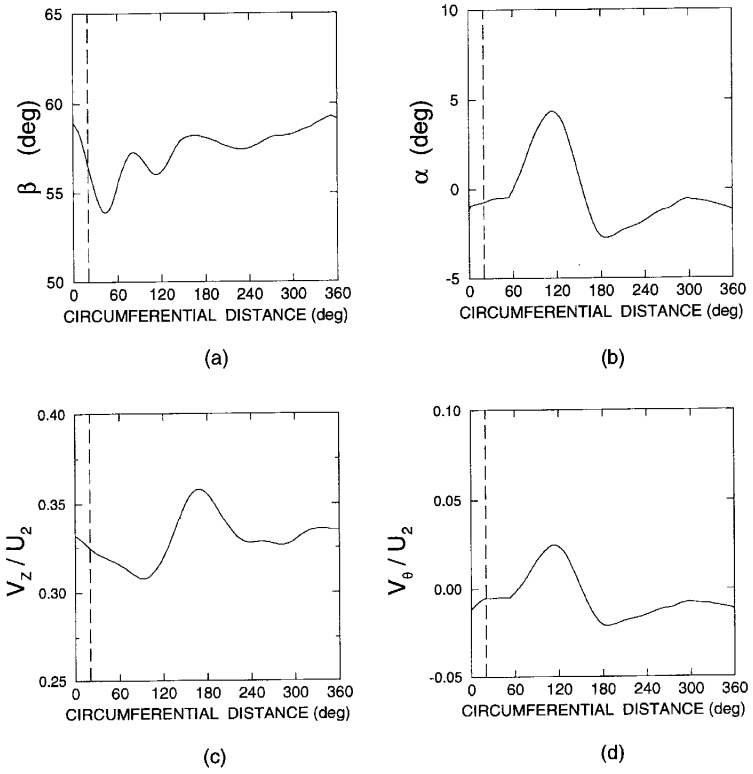

Figure 9: Circumferential variation of mass averaged $\beta_1, \alpha_1, V_{Z1}, V_{\theta 1}$, at leading edge, S_r = 0.22 for the lower mass flow case (- - - tongue position).

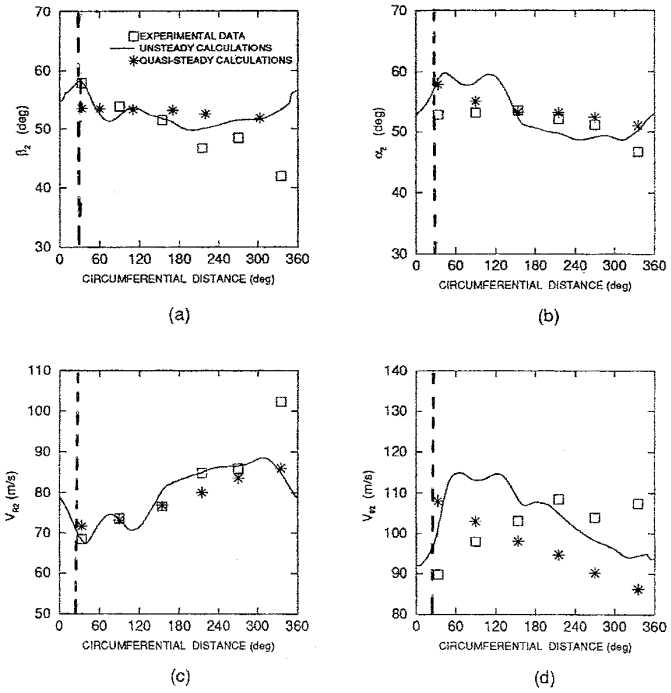

Figure 10: Circumferential variation of mass averaged $\beta_2, \alpha_2, V_{R2}, V_{\theta 2}$ at R/R$_2$=1.10, Sr=0.22, for the higher mass flow case (- - - tongue position).

streamsurfaces is not shown here but it has also a wavy variation with periodicity of one impeller rotation, similar to the one observed at lower than optimum mass flow. The flow unsteadiness inside the impeller repeats itself after a period of the phenomenon, as it was also concluded in [16]

The circumferential variation of the mass averaged relative flow angle β_2, absolute flow angle α_2, radial velocity V_{R2} and absolute tangential velocity $V_{\theta 2}$ at *R/R2* = 1.10 are compared to the steady flow solution in Figure 10. In this figure stars show results obtained from steady flow calculations, in which the local static pressure is imposed at the outlet. They show a monotonic increase or decrease with the outlet static pressure, but completely fail to capture the large local variations of the flow parameters. Squares show experimental results available in the literature [2]. The numerical predictions of the unsteady flow model show a fair agreement with the measurements, taking into account the complexity of the phenomenon. Possible explanation of the discrepancies can be attributed to the fact that downstream the trailing edge of the blades, at *R/R2* = 1.10, there is the formation of the jet and wake structure [1] affecting the slip factor of the blades and all the flow variables. The numerical model used in the present study cannot take into account this effect.

One observes again a 2 wave per rotation variation. The first peak in β_2 occurs at 35^o (Figure 10a). It is due to the peak in exit static pressure shown in Figure 3. This variation shows a small phase shift when compared to the variation of V_{R2} and α_2, whose variations are closely related to each other.

All variations show again a 2-period per rotation behaviour as a result of the pressure waves reflected at the leading edge, travelling twice upstream and downstream the impeller during one rotation. This was also observed for the case of full-bladed centrifugal impeller operating at higher than optimum mass flows and a similar value of the acoustic Strouhal number, in [8]. The two waves per rotation were even more clearly visible because the waves were not perturbed by reflections at the leading edge of the splitter vanes.

The circumferential variation of the mass averaged $\beta_1, \alpha_1, V_{Z1}, V_{\theta 1}$ at leading edge position is shown in Figure 11. A minimum in the axial flow velocity V_{Z1} is observed at 120^o. This occurs at a $\Delta\theta$ = 90^o later than the minimum value of V_{R2}. This shift corresponds to the time needed by a perturbation to travel upstream over a length L. One can conclude from this that there is no direct interaction between the high downstream static pressure and the high relative flow angle at θ = 50^o.

Observing the β_2 distributions for the case of lower mass flows (in Figure 8a), as well as for the case of higher mass flows (in Figure 10a), one can conclude that the assumption of circumferentially constant *β2*, made in many 1*D* models (such as [4]), is not in agreement with reality. This is, in the authors' opinion, the main source of errors in 1*D* models at higher reduced frequency or acoustic Strouhal number.

The importance of the pressure waves, travelling upstream and downstream, applies only to compressible flows. The use of the rigid column theory remains a good approximation for incompressible flows.

3. Conclusions

The present model solving the 3*D* unsteady Euler equations can give valuable information about unsteady flows in impellers at an affordable computer time and cost.

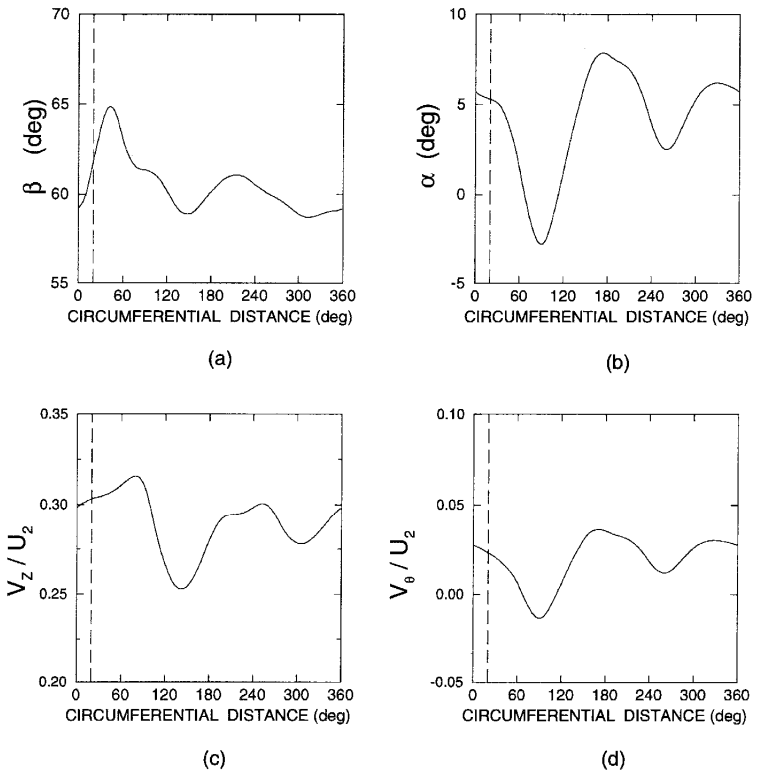

Figure 11: Circumferential variation of mass averaged $\beta_1, \alpha_1, V_{Z1}, V_{\theta 1}$ at leading edge, S_r=0.22, for the higher mass flow case (- - - tongue position).

Calculations of the relative blade Mach number distribution in the splitter-vaned impeller show that the flow unsteadiness is governed by pressure waves propagating in the blade to blade channels.

Different response to the outlet static pressure distortion by the upper and lower channels between two main blades is observed. More specifically, the channel between the main blade suction side and the splitter vane pressure side is more loaded than the channel between the splitter suction side and the main blade pressure side. Such a conclusion was never reported in the past.

The variation of the impeller outlet flow is much larger than the one obtained from quasisteady calculations although the acoustic Strouhal number is only 0.22. The latter are applicable only in cases of very low Strouhal numbers, $Sr < 0.1$.

Strong circumferential variations of the outlet relative flow angle β_2 show that the assumption of constant outlet relative flow angle, used in many existed 1*D* models, is incorrect. Circumferential variations in β_2 at higher and lower mass flows were experimentally observed [14, 15]. Circumferential variations in the absolute tangential velocity at the impeller exit indicate slip factor variations during one rotation. Variations in the radial velocity show local mass flow variations.

The flow perturbation extends upstream of the impeller and creates significant variations of the flow at the leading edge region for both higher and lower than optimum mass flows.

When comparing the variations in flow quantities at leading edge, at R/R_2=1.10, as well as the blade relative Mach number distributions at lower and higher mass flows, one can see that the variations in the latter case are larger than in the former one, although the imposed static pressure distribution has the same amplitude for both cases. This means that static pressure distortions at higher mass flows have a larger effect on the impeller flow, than distortions at lower mass flows. Navier-Stokes computations reported in the literature [17] are time consuming and require large computational effort. They can provide valuable information if they are coupled with experimental data, fact that allows the correct tuning of the empirical coefficients included in the turbulence models.

References

[1] A. Whitfield, N.C. Baines. Design of Radial Turbomachines. Longman Group UK Limited; 1990.

[2] M. Sideris. Circumferential distortion of the flow in Centrifugal Compressors due to Outlet Volutes. PhD.Thesis, RUG-Von Karman Institute, 1988.

[3] H. Pfau, ''Temperaturmessungen zur Stromungsuntersuchung, insbesondere an Radialverdichtern''. Konstruktion, Heft 12, 1967, 478-484.

[4] J.A. Lorett, S. Gopalakrishnan, ''Interaction in between Impeller and Volute of Pumps at off-design conditions''. ASME Journal Fluids Engineering. Vol. 108, 1986.

[5] H. Uchida, M. Inayoshi, K. Sugiyama, ‘‘Effect of a Circumferential Static Pressure Distortion on Small-Sized Centrifugal Compressor Performance.’’ International Gas Turbine Congress held in Tokyo, Japan, 1987.

[6] R. Badie, J.B. Jonker, T.G. van Essen, ‘‘Calculations on the Time-Dependent Potential Flow in a Centrifugal Pump’’ ASME Paper 92-GT-151.International Gas Turbine and Aeroengine Congress and Exposition in Cologne, Germany, 1992.

[7] D. Croba. Modélisation de l’écoulement instationnaire dans les pompes centrifuges. Interaction roue-volute. PhD.Thesis, Institut National Polytechnique de Grenoble, 1992.

[8] A. Fatsis. Computation of the 3-Dimensional Unsteady Flow in a Centrifugal Impeller due to a downstream Static Pressure Circumferential Distortion. PhD.Thesis, RUG-Von Karman Institute, 1995

[9] A. Fatsis, ‘‘Three dimensional unsteady flow calculations in radial components”. von Karman Institute Lecture Series 1993-01 ‘Spacecraft Propulsion’, 1993

[10] M. Murakami, K. Kikuyama, E. Asakura, ‘‘Velocity and Pressure distributions in the impeller passages of Centrifugal Pumps’’, Journal of Fluids Engineering, Vol. 102, 1980, 420-426.

[11] K. Kikuyama, K. Minemura, Y. Hasegawa, E. Asakura, M. Murakami, ‘‘Unsteady pressure distributions on the impeller blades of a centrifugal pump-impeller operating off-design’’. ASME Paper No. 87-GT-144, 1987.

[12] N. Bulot and I. Tribinjac,“Impeller-diffuser interaction: analysis of the unsteady flow structures based on their direction of propagation”. Proceedings of the 8th International Symposium on Experimental and Computational Aerothermodynamics of Internal Flows Lyon, July 2007.

[13] K.U.Ziegler, H.E.Gallus, and R.Niehuis, “A Study on Impeller-Diffuser Interaction—Part I: Influence on the Performance”, ASME Journal of Turbomachinery Vol. 125, No. 1, 2003, 173-183.

[14] T. Meakhail and S. O. Park, “A Study of Impeller-Diffuser-Volute Interaction in a Centrifugal Fan“. ASME Journal of Turbomachinery, Vol.127, No. 1, 2005, 84-91.

[15] H.-P.Dickmann, T.S.Wimmel, J.Szwedowicz, D.Filsinger, and C.H.Roduner, “Unsteady Flow in a Turbocharger Centrifugal Compressor: Three-Dimensional Computational Fluid Dynamics Simulation and Numerical and Experimental Analysis of Impeller Blade Vibration”. J. Turbomachinery, Vol. 128, No. 3, 455-466.

[16] K. Majidi, “Numerical Study of Unsteady Flow in a Centrifugal Pump”. ASME Journal of Turbomachinery, Volume 127, No. 2, 2005, 363-372

[17] M Younsi, F Bakir, S Kouidri, R Rey, ‘‘Numerical and experimental study of unsteady flow in a centrifugal fan”. Proceedings of the Institution of Mechanical Engineers, Part A: Journal of Power and Energy, Vol. 221, No. 7, 2007, 1025-1036.